scientific reports

Check for updates

OPEN

Advanced study of wavy dynamical behavior of suspended living organisms in generalized nanomaterials with magnetic and buoyancy effects

Latif Ahmad[1], Saleem Javed[1], Bahadar Zeb[1], Umair Khan[2,3], Najiyah Safwa Khashi'ie[4], Samia Elattar[5] & Hounkonnou Oliver Holali[6]✉

This study presents a novel mathematical framework to investigate the undulating flow of a Cross fluid containing gyrotactic microorganisms under bioconvection. The problem is important because microorganism-induced density gradients can significantly influence momentum, heat, and mass transport in biological and engineering systems, such as microfluidic devices and nanofluid-based thermal management. The novelty of this work lies in simultaneously analyzing the effects of key parameters Peclet number, Rayleigh number, and magnetic field strength on drag force, heat and solute transport rates, and microorganism density, extending beyond previous studies that considered only partial effects. The transformed nonlinear boundary value problem is solved numerically using an improved bvp4c algorithm, which enhances computational stability and accuracy compared to conventional approaches. The results indicate that increasing the Péclet and Rayleigh numbers leads to a notable reduction in drag force and in the rates of heat and mass transfer. Moreover, higher values of the magnetic field parameter and Rayleigh number cause a significant decrease in the Sherwood number, demonstrating their strong influence on solute transport. The outcomes are presented through detailed graphical analyses and validated by comparison with previously published studies, confirming the reliability of the improved numerical method and the consistency of the physical model.

Keywords Bioconvection, Energy conservation, Electrical conductivity, Gyrotactic microorganisms, Cross fluid

Abbreviations

$\overline{a}$	Amplitude of surface waviness m $[\mathrm{L}]$
$\mathrm{B_o}$	Magnetic field strength T (tesla) $\left[\mathrm{MA^{-1}T^{-2}}\right]$
$\mathrm{b_c}$	Chemotaxis constant m $[\mathrm{L}]$
C	Solute concentration $\mathrm{kgm^{-3}}$ $\left[\mathrm{mL^{-3}}\right]$
$\mathrm{C_f}$	Skin friction coefficient
$\mathrm{c_p}$	Specific heat at constant pressure $\mathrm{jkg^{-1}K^{-1}}$ $\left[\mathrm{L^2T^{-2}K^{-1}}\right]$
$\mathrm{D_B}$	Brownian diffusion coefficient $\mathrm{m^2s^{-1}}$ $\left[\mathrm{L^2T^{-1}}\right]$
$\mathrm{D_n}$	Diffusion coefficient of microorganisms $\mathrm{m^2s^{-1}}$ $\left[\mathrm{L^2T^{-1}}\right]$

[1]Department of Mathematics, Shaheed Benazir Bhutto University, Sheringal Dir Upper 18000, Pakistan. [2]Department of Mathematics, Saveetha School of Engineering, Saveetha Institute of Medical and Technical Sciences, Saveetha University, Chennai 602105, Tamil Nadu, India. [3]Department of Mathematics, Faculty of Science, Sakarya University, Serdivan/Sakarya 54050, Turkey. [4]Fakulti Teknologi Dan Kejuruteraan Mekanikal, Universiti Teknikal Malaysia Melaka, Hang Tuah Jaya, , 76100 Durian Tunggal, Melaka, Malaysia. [5]Department of Industrial and Systems Engineering, College of Engineering, Princess Nourah bint Abdulrahman University, P.O. Box 84428, Riyadh 11671, Saudi Arabia. [6]Department of Mathematics, University of Kara, P.O. Box 43, Kara, Togo. ✉email: allicouture08@gmail.com

D_s	Solutal diffusivity m^2s^{-1} $\left[L^2T^{-1}\right]$
	Dimensionless stream function
g	Gravitational acceleration ms^{-2} $\left[LT^{-2}\right]$
h	Dimensionless nanoparticle concentration
j_w	Wall solute mass flux $kgm^{-2}s^{-1}$ $\left[ML^{-2}T^{-1}\right]$
j_{np}	Nanoparticle mass flux $kgm^{-2}s^{-1}$ $\left[ML^{-2}T^{-1}\right]$
j_n	Motile microorganism flux $m^{-2}s^{-1}$ $\left[L^{-2}T^{-1}\right]$
k	Thermal conductivity $Wm^{-1}K^{-1}$ $\left[MLT^{-3}K^{-1}\right]$
L	Characteristic length m [L]
Le	Lewis number
Ln	Bioconvective Lewis number
M	Microorganism concentration m^{-3} $\left[L^{-3}\right]$
m	Magnetic parameter
n	Power-law index
Nc	Buoyancy ratio parameter
Nb	Bioconvection constant (motility parameter)
Nr	Radiation parameter
NSh	Nanoparticle Sherwood number
Nu	Nusselt number (heat transfer rate)
Pe	Peclet number
Pr	Prandtl number
Q	Dimensionless motile microorganism density number
q_w	Wall heat flux Wm^{-2} $\left[MT^{-3}\right]$
Rb	Bioconvection Rayleigh number
Re	Reynolds number
Ri	Richardson number
Sh	Sherwood number (solute mass transfer rate)
T	Temperature K [K]
T_w, T_∞	Wall and ambient temperatures K [K]
u, v	Velocity components along x and y axes ms^{-1}[LT^{-1}]
U_∞	Free-stream velocity $ms^{-1}\left[LT^{-1}\right]$
We	Weissenberg number
V_c	Average swimming velocity of microorganisms $ms^{-1}\left[LT^{-1}\right]$
x, y	Cartesian coordinates m[L]
$_c$	Solutal expansion coefficient
$_T$	Thermal expansion coefficient$K^{-1}\left[K^{-1}\right]$
χ	Dimensionless microorganism density
η	Dimensionless similarity variable
μ	Dynamic viscosity Pa.s$\left[ML^{-1}T^{-1}\right]$
ϕ	Dimensionless solute concentration
Φ	Nanoparticle volume fraction
ψ	Stream function m^2s^{-1} $\left[L^2T^{-1}\right]$
ρ	Fluid density kgm^{-3} $\left[ML^{-3}\right]$
$\widehat{\sigma}(\hat{x})$	Wavy surface function m [L]
σ_x	Derivative of wavy surface function
τ_w	Wall shear stress Nm^{-2} $\left[ML^{-1}T^{-2}\right]$
θ	Dimensionless temperature

Generalized Newtonian fluids (GNFs) represent a widely encountered category of non-linear fluids, commonly observed in fields such as petroleum engineering, suspension systems, as well as polymer solutions. These fluids are characterized by their apparent viscosity, which varies in response to shear strain. Numerous constitutive models have been proposed to describe their shear rate-dependent rheological behavior, including the power-law, Sisko, as well as Carreau-Yasuda models. A notable subclass within GNFs is the Cross fluid, originally introduced by Cross[1]. The Cross model effectively addresses issues that arise at elevated shear rates and has found extensive use in engineering simulations, industrial applications, and biological systems. For instance, Nazeer et al.[2] elaborated the non-linear nanofluids under the influence of thermal radiation as well as internal heat generation or absorption. Sabir et al. [3] studied the effects of thermal radiation and activation energy on non-Newtonian fluid flow under an inclined magnetic field. The experimental work of Escudier et al.[4] provided validation for the Cross model and valuable insights into its rheological characteristics. In a recently, Ali and Das[5] explored the movement of blood infused with modified tri-hybrid nanoparticles featuring interfacial nanolayers within a diseased, ciliated arterial channel. Their study incorporated electroosmotic influences, magnetic (Lorentz) forces, and predictive frameworks based on neural computation and fractional-order

modeling. Adhikari et al.[6] analyzed the behavior of microorganisms in a Cross-type blood flow enriched with tetra-hybrid nanoparticles through a flexible, stenosed artery, accounting for magnetic interactions and slip conditions at the wall using a neural-network-driven scheme. Furthermore, Kumar et al.[7] investigated the heat-transfer performance of penta-hybrid nanoparticle-laden blood flowing through fin-like geometries, employing deep learning techniques alongside a finite-difference numerical strategy.

Mixed convection flow over vertical surface is of significant interest in many industrial as well as environmental processes, such as solar collector, heat exchangers, electronic cooling devices as well as geophysical flows. When the surface under consideration is non-flat, specifically wavy the complexity of the flow and heat transfer behavior increases due to the induced geometric perturbations, which can significantly alter the boundary layer structure. In these settings, mixed convection emerges from the combined effects of thermal buoyancy and externally imposed (forced) convection. The presence of a vertical wavy surface adds complexity by inducing additional shear and pressure gradients, which in turn generate flow recirculation and alter the temperature distribution. Such surfaces are often employed to enhance convective transport and play a crucial role in influencing heat transfer rates and surface shear stress (skin friction).The coupled convection across a wavy wall was researched by Moulic and Yao[8]. Jang and Yan[9] reported the combined convective heat-mass transfer across a wavy wall that is perpendicular. In the existence of a magnetic field, Wang and Chen[10] were able to develop numerical solutions for the mixed convection BL flow issue on inclined wavy plates. The cooling performance of a moving wavy surface was investigated by Mehmood et al.[11] utilising magnetohydrodynamic (MHD) nanofluid flow. Iqbal et al.[12] investigated the movement of nanofluids across a complicated wavy wall, taking into account the permeability of porous media and magnetic field behaviours. Acharya[13] investigated the hydrothermal behavior and entropy characteristics of buoyancy-driven MHD hybrid nanofluid flow within a finned octagonal enclosure, highlighting its relevance to thermal energy storage applications. The study by Ahad et al.[14] focused on the thermosolutal magnetohydrodynamic convection behavior of a hybrid $MWCNT - Fe_3O_4$ nano-liquid flowing past a wavy wall, with particular attention to the effects of heat as well as mass fluxes applied at the wall. Moreover, wave-related phenomena find broad application in geophysical studies. Zhang et al.[15] analyzed the transfer of kinetic energy between near-inertial waves and mesoscale eddies or diurnal tides during Typhoon Rai, thereby enhancing understanding of the processes that regulate energy distribution within the ocean. Acharya[16] examined the influence of curved fins on entropy generation and hydrothermal variations in buoyancy-driven MWCNT–Fe_3O_4–H_2O hybrid nanofluid flow within an annular enclosure. Zhang et al.[17] numerically analyzed a 3D integrated configuration comprising an inertial built-in wave energy converter array in combination with a floating breakwater.

Bioconvection refers to the collective movement of large populations of motile microorganisms within a fluid, most commonly free-swimming species such as zooplankton in aquatic settings. In recent years, bioconvection has gained increasing importance in areas such as blood-flow modeling, biosensing, micro-enzyme systems, nanobiotechnology as well as biomedical instrumentation. These advances have strengthened research related to drug-delivery mechanisms, pharmacokinetics, constituent detection, and nanomedicine within biological as well as biotechnological applications. The concept of bioconvection was initially introduced by Wager[18]. Ahmed and Mahdy[19] investigated the transport behavior of a gyrotactic microorganism-laden nanofluid undergoing laminar MHD natural convection over a vertically oscillating surface embedded in a non-Darcian porous medium. Srinivasacharya and Ramana[20] analyzed the influence of thermal radiation as well as double-diffusion effects on the bioconvective flow of a nanofluid across an inclined wavy surface. Adhikari and Das[21] studied microorganism transport in a magnetically actuated, reactive Casson-Maxwell nanoliquid flowing over an inclined elastic cylinder, with emphasis on entropy generation. Sarkar and Das[22] examined the motion of gyrotactic microorganisms in a magnetically influenced Sutterby nanofluid over a translating cylinder situated within a Darcy-Forchheimer porous medium, incorporating Arrhenius reaction kinetics. Adhikari and Das[23] explored the dynamics of motile microorganisms in a chemically reactive, magnetically influenced Casson-Maxwell-Oldroyd-B nanofluid over an inclined extended cylindrical surface, focusing on entropy-generation analysis.

Extensive research has focused on MHD natural convection accompanied by heat as well as mass transport in electrically conductive fluids, owing to its relevance in diverse areas such as power-generation systems, atmospheric science, solar as well as astrophysical studies, chemical processing, and geophysical flows. Khan et al.[24] analyzed how variations in magnetic intensity, reactive species, volumetric heat production, and Newtonian heating influence the convective behavior of Casson fluid moving past a vertically translating plate situated within a porous structure. Muhammad et al.[25] explored magneto-natural convection in vertically aligned concentric annuli, highlighting the implications of heat absorption under the combined effects of radially imposed as well as induced magnetic fields. Ramasekhar et al.[26] examined the thermofluidic characteristics of engine lubricant blended with copper nanoparticles over a rotating disk while accounting for simultaneous binary chemical reactions. Magnetic field generators are essential tools in biomedical engineering, supporting applications such as targeted drug delivery, magnetic stimulation, and imaging. To further expand these capabilities, researchers are developing systems that offer greater efficiency and tunability. Lei et al.[27] presented a parallel resonant magnetic field generator tailored for biomedical use, demonstrating a highly effective method for generating controlled magnetic fields suitable for therapeutic and medical applications. Palencia et al.[28] employed an ANFIS–PSO hybrid strategy to assess axisymmetric flow behavior of a Cu–CNT–Graphene–TiO_2 tetra-hybrid nanofluid mixed with WEG–blood under linear thermal radiation as well as an oblique magnetic field, with emphasis on biomedical utility. Bhattacharyya et al.[29] studied the MHD response of magnetic nanofluids inside mini-channel heat sinks, targeting performance enhancement for electronic cooling applications. Pooja et al.[30] demonstrated improved thermal transport in penta-hybrid nanofluid motion over an extending surface using the homotopy perturbation technique integrated with an artificial neural network model. Kumar et al.[31] utilized the Levenberg–Marquardt optimization framework to predict heat and mass transport augmentation in

magnetically influenced non-Newtonian nanofluids, taking into account activation energy and bioconvective effects. Ramasekhar et al.[32] numerically assessed Casson hybrid nanofluid motion over a stretching cylindrical configuration, underscoring the major influence of internal heat sources as well as sinks.

Novelty of the work

This study provides a comprehensive investigation of Cross fluid flow containing gyrotactic microorganisms under bioconvection over a vertical wavy surface, addressing a notable gap in the existing literature, where most studies focus on flat surfaces or examine only partial aspects of transport phenomena. The novelty of this work lies in its analysis of the coupled effects of momentum, heat, and mass transfer influenced by microorganism density gradients**,** offering detailed insights into bioconvective accumulation and the undulating flow behavior near complex surfaces. Furthermore, the study employs a robust numerical approach, specifically an improved bvp4c method**,** which ensures enhanced stability and accuracy in solving strongly nonlinear boundary value problems. By combining a rigorous physical model with an advanced computational technique, this research provides a deeper understanding of non-Newtonian bioconvective flows and delivers results that are both practically relevant and distinct from previous studies.

Problem formulation

The boundary layer analysis presented here is formulated to accommodate an arbitrary variation in the surface function, $\widehat{\sigma}(\widehat{x})$, allowing for general applicability to vertical wavy surface. For the purposes of the present numerical study, however, the surface is assumed to exhibit sinusoidal deformations, which are commonly used in the literature to model wavy boundaries due to their mathematical tractability and physical relevance. The subsequent description focuses on a representative portion of the wavy surface, consistent with approaches adopted in previous studies Mehmood et al.[11] as well as Iqbal et al.[12] thereby providing a clear framework for the analysis and ensuring that the results can be meaningfully compared with established work.

$$\overline{y}_w = \overline{a}\sin\left(\frac{\pi\overline{x}}{L}\right). \tag{1}$$

The vertical surface is subjected to the force of gravity, which significantly affects the flow behavior. The velocity components of the fluid (liquid) are represented by $\overline{u}(\overline{x}, \overline{y})$ as well as $\overline{v}(\overline{x}, \overline{y})$, corresponding to the velocity in the vertical $(\overline{x})$ and horizontal $(\overline{y})$ directions, respectively and is presented through Fig. 1 as;

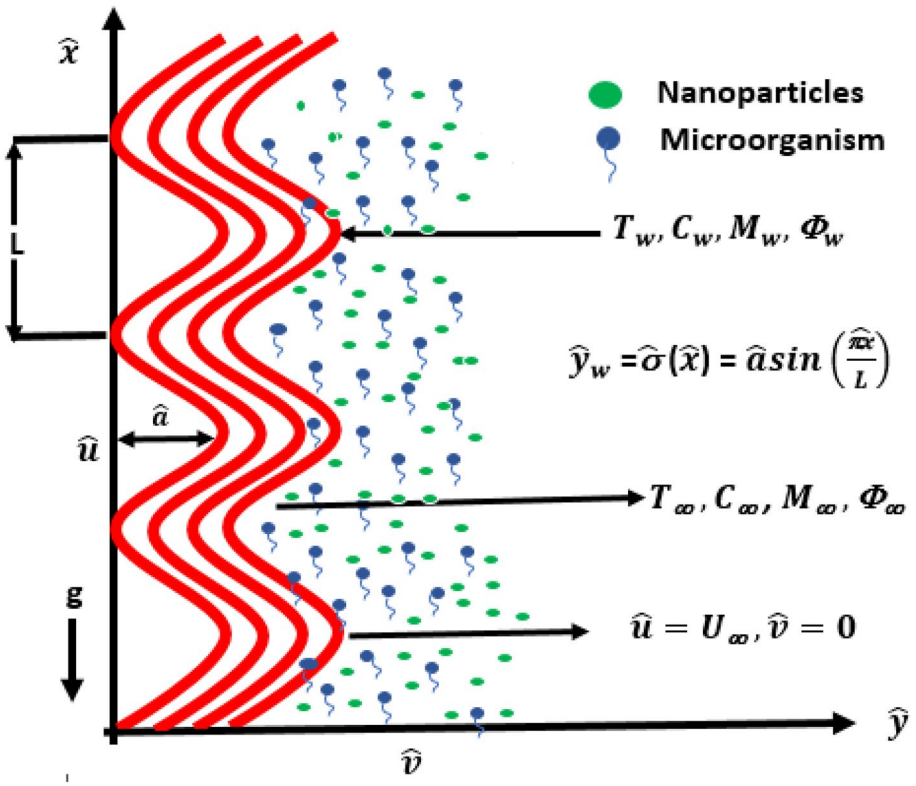

Fig.1. Geometry with 2-D coordinate system.

Assumptions (in chronological order)

The flow is considered steady, laminar as well as incompressible.
The flow is assumed to be 2D and characterized by a wavy pattern.
The fluid follows the Cross fluid model, exhibiting non-Newtonian behavior.
A uniform magnetic field of strength B_o is applied perpendicular to the surface, influencing the motion of the electrically conducting fluid.
The velocity boundary condition at the surface is defined by a prescribed surface velocity profile.
The ambient (free-stream) temperature and concentration are denoted by T_∞ as well as C_∞, respectively.
The surface temperature and concentration are represented by T_w as well as C_w, respectively.
The concentrations of motile microorganisms at the surface as well as in the free stream are symbolized as M_w as well as M_∞, respectively.
The system of governing PDEs is derived based on the above assumptions and later transformed into non-dimensional form for numerical analysis.

The essential conservation equations employed in this analysis are adopted from the formulations in (Mehmood et al.[11], Iqbal et al.[12] and Ahad et al.[14]) and are given as follows.

$$(\overline{u}_{\overline{x}} + \overline{v}_{\overline{y}}) = 0, \tag{2}$$

$$\left[\begin{array}{c} \frac{1}{\rho}\left(\overline{u}\overline{u}_{\overline{x}} + \overline{v}\overline{u}_{\overline{y}}\right) + \overline{p}_{\overline{x}} = \beta_C \rho_{f_\infty} g(1-\varphi_\infty)(C-C_\infty) - \sigma_o B_o^2 \overline{u} \\ -g(\rho_p - \rho_{f_\infty})(\varphi - \varphi_\infty) - \beta_M \rho_{f_\infty} g(\rho_m - \rho_{f_\infty})(M - M_\infty) + \beta_T \rho_{f_\infty} g(1-\varphi_\infty)(T-T_\infty) \\ + \frac{\partial}{\partial \overline{y}}\left[\frac{\overline{u}_{\overline{y}} + \overline{v}_{\overline{x}}}{1+\left\{\Gamma^2\left(4\overline{u}_{\overline{x}}^2 + \left(\overline{u}_{\overline{y}} + \overline{v}_{\overline{x}}\right)^2\right)\right\}^{\frac{n}{2}}}\right]\mu + \frac{\partial}{\partial \overline{x}}\left[\frac{2\mu \overline{u}_{\overline{x}}}{1+\left\{\Gamma^2\left(4\overline{u}_{\overline{x}}^2 + \left(\overline{u}_{\overline{y}} + \overline{v}_{\overline{x}}\right)^2\right)\right\}^{\frac{n}{2}}}\right] \end{array}\right], \tag{3}$$

$$\left[\begin{array}{c} \frac{1}{\rho}\left(\overline{u}\overline{v}_{\overline{x}} + \overline{v}\overline{v}_{\overline{y}}\right) + \overline{p}_{\overline{y}} = \frac{\partial}{\partial \overline{x}}\left[\frac{\overline{u}_{\overline{y}} + \overline{v}_{\overline{x}}}{1+\left\{\Gamma^2\left(4\overline{u}_{\overline{x}}^2 + \left(\overline{u}_{\overline{y}} + \overline{v}_{\overline{x}}\right)^2\right)\right\}^{\frac{n}{2}}}\right]\mu + \frac{\partial}{\partial \overline{y}}\left[\frac{2\mu \overline{v}_{\overline{y}}}{1+\left[\Gamma^2\left(4\overline{u}_{\overline{x}}^2 + \left(\overline{u}_{\overline{y}} + \overline{v}_{\overline{x}}\right)^2\right)\right]^{\frac{n}{2}}}\right] \end{array}\right], \tag{4}$$

$$\overline{u}T_{\overline{x}} + \overline{v}T_{\overline{y}} - \frac{k}{\rho c_p}\left(T_{\overline{x}\overline{x}} + T_{\overline{y}\overline{y}}\right) = 0, \tag{5}$$

$$D_B\left(\Phi_{\overline{x}\overline{x}} + \Phi_{\overline{y}\overline{y}}\right) = \overline{u}\Phi_{\overline{x}} + \overline{v}\Phi_{\overline{y}}, \tag{6}$$

$$\overline{u}C_{\overline{x}} + \overline{v}C_{\overline{y}} - D_S\left(C_{\overline{x}\overline{x}} + C_{\overline{y}\overline{y}}\right) = 0, \tag{7}$$

$$\overline{u}M_{\overline{x}} + \overline{v}M_{\overline{y}} + \left(M\overline{V}\right)_{\overline{x}} + \left(M\overline{V}\right)_{\overline{y}} - D_n\left(M_{\overline{x}\overline{x}} + M_{\overline{y}\overline{y}}\right) = 0. \tag{8}$$

Here, $\overline{V}$ represents the average swimming velocity vector of the microorganisms, where $\overline{V} = \frac{q_n D_S b_c W_c}{q_{np} D_n M_\infty}\frac{\partial \varphi}{\partial \overline{y}}$. In this expression, b_c represents constant for the chemotaxis and W_c denotes the swimming speed of the cells. The limitations that apply are;

$$\left[\begin{array}{c} \overline{u} = U_\infty, \overline{v} = 0, (M - M_w) = (\varphi - \varphi_w) = (T - T_w) = (C - C_w) = 0 \text{ at } \overline{y} = \overline{y}(w), \\ \\ \overline{u} = 0, (T - T_\infty) \to (M - M_\infty) \to (C - C_\infty) \to (\varphi - \varphi_\infty) \to 0 \text{ as } \overline{y} \to \infty. \end{array}\right]. \tag{9}$$

By using the succeeding dimensionless variables, which are specified in (Jang and Yan[9] Mehmood et al.[11], Iqbal et al.[12] and Ahad et al.[14]), and by adhering to the boundary layer technique. Equations (2–8) then take on the following structure:

$$u_x + v_y = 0, \tag{10}$$

$$\left[\begin{array}{c} uu_x + vu_y - \frac{1}{1+\sigma_x^2}\left[-\frac{\partial p}{\partial x} - \sigma_x \sigma_{xx} u^2 + Ri\left(\theta + N_c\varphi - N_r h - R_b\chi\right)\right] \\ = \left(1+\sigma_x^2\right)\frac{1-(1+n)\left(We\left(1+\sigma_x^2\right)u_y\right)^n}{\left[1+\left(We\left(1+\sigma_x^2\right)u_y\right)^n\right]^2}u_{yy} - mu \end{array}\right], \tag{11}$$

$$u\theta_x + v\theta_y - \frac{1}{\mathrm{Pr}}\left(1+\sigma_x^2\right)\theta_{yy} = 0, \tag{12}$$

$$uh_x + vh_y - \frac{1}{Le}\left(1+\sigma_x^2\right)h_{yy} = 0, \tag{13}$$

$$u\varphi_x + v\varphi_y - \frac{1}{Ln}\left(1+\sigma_x^2\right)\varphi_{yy} = 0, \tag{14}$$

$$u\chi_x + v\chi_y + \frac{Pe}{Sc}\left((A+\chi)\left(1-\sigma_x\right)\varphi_{yy} + \varphi_y\chi_y\right) - \frac{1}{Sc}\left(1+\sigma_x^2\right)\chi_{yy} = 0. \tag{15}$$

Notations	Parameter values	Mathematical discription
We	$\Gamma \frac{U_\infty}{L} Re^{1/2}$	Weissenberg number
Ri	$\frac{Gr}{Re^2}$	Richardson number
R_b	$\frac{\beta_M \left(\rho_m - \rho_{f_\infty}\right)(M_w - M_\infty)}{\rho_{f_\infty} \beta_T (1-\varphi_\infty)(T_w - T_\infty)}$	Rayleigh number
L_n	$\frac{\nu}{D_s}$	Lewis number for nano-particle
N_c	$\frac{\beta_C (\Delta C)}{\rho_{f_\infty} \beta_T (\Delta T)}$	Regular double particle
N_r	$\frac{\left(\rho_p - \rho_{f_\infty}\right)(\Phi_w - \Phi_\infty)}{\rho_{f_\infty} \beta_T (1-\varphi_\infty)(T_w - T_\infty)}$	Buoyancy ratio factors
Pr	$\frac{k}{\mu c_p}$	Prandtl number
Sc	$\frac{\nu}{Dn}$	Schmidt number
Pe	$\frac{b_C w_C}{Dn}$	Peclet number
A	$\frac{M_\infty}{M_w - M_\infty}$	Bio-convection constant
L_e	$\frac{\nu}{D_B}$	Lewis number
m	$\frac{\sigma_o (B_o L)^2}{\upsilon Re}$	Magnetic Factor

Table 1. Symbols and description of the controlling parameters.

Furthermore, the above Eqs. (11) to (15) comprised distinct influential or controlling parameters. These parameters are namely and mathematically defined in Table 1.

The boundary conditions (BCs) are;

$$\left[\begin{array}{c} u = 1, h = \varphi = 1, v = 0, \theta = 1, \chi - 1 = 0 \text{ at } y = \sigma(x) \\ u = 0, h = 0, \varphi = 0, \theta = 0, \chi = 0 \; as \; y \to \infty \end{array}\right]. \tag{16}$$

A system of nonlinear PDEs is formed by Eqs. (11–15) and is subject to the boundary conditions specified in Eq. (16). These equations can be solved using any suitable method. Using the transformation outlined in (Jang and Yan[9], Mehmood et al.[11], Iqbal et al.[12]), the set of equations plus BCs may be converted into an appropriate form in order to expedite the computation process:

$$u = \psi_y, v = -\psi_x, \psi = x^{1/2} f(\eta), \eta = (x^{-1/2}) y, x = \xi, \tag{17}$$

$$\begin{aligned} &\left(\left(1+\sigma_x^2\right)\left[1+(1-n)\left(We\left(1+\sigma_x^2\right)\xi^{\frac{-1}{2}} f''\right)^n\right]\right)\left(1+\left\{We\left(1+\sigma_x^2\right)\xi^{\frac{-1}{2}} f''\right\}^n\right)^{-2} f''' \\ &-\xi \frac{\sigma_x \sigma_{xx}}{1+\sigma_x^2} f'^2 - \frac{\xi}{\left(1+\sigma_x^2\right)} m f' + 0.5 f f'' + \frac{1}{\left(1+\sigma_x^2\right)}\left(Ri\left(\theta + N_c \varphi - N_r h - R_b \chi\right)\right) = 0, \end{aligned} \tag{18}$$

$$\left(1+\sigma_x^2\right)\theta'' + \frac{1}{2}\,\mathrm{Pr}\, f\theta\prime = 0, \tag{19}$$

$$\left(1+\sigma_x^2\right)h'' + \frac{1}{2} Lef h' = 0, \tag{20}$$

$$\left(1+\sigma_x^2\right)\varphi'' + \frac{1}{2} Lnf\varphi' = 0, \tag{21}$$

$$\frac{1}{Sc}\left(1+\sigma_x^2\right)\chi'' = -\frac{1}{2}\chi' f + (1-\sigma_x)\frac{Pe}{Sc}\left((A+\chi)h'' + h'\chi'\right). \tag{22}$$

The requirements for the BCs are

$$\left[\begin{array}{c} f = 0, (f' - 1) = 0, \theta = h = \varphi = \chi = 1, \eta = 0 \\ f' = 0, \theta = 0, h = 0, \varphi = 0, \chi = 0, \eta \to \infty \end{array}\right]. \tag{23}$$

Engineering quantities

The key engineering parameters to be evaluated in this study include the skin friction coefficient, Nusselt, Sherwood, nanoparticle Sherwood as well as the motile microorganism density numbers**.** These quantities represent the wall shear stress, rates of heat transfer, mass transfer, nanoparticle mass transfer as well as motile microorganism flux, respectively, and can be calculated from the corresponding wall gradients of velocity, temperature, solute concentration, nanoparticle concentration as well as microorganism density (Jang and Yan[9], Mehmood et al.[11], Iqbal et al.[12]).

	$m = 0.01$			$m = 0.1$		
	Mehmood et al.[11]	Iqbal et al.[12]	Present work	Mehmood et al.[11]	Iqbal et al.[12]	Present work
ξ	$f''(\xi,\eta)_{\eta=0}$	$f''(\xi,\eta)_{\eta=0}$	$f''(\eta)_{\eta=0}$	$f''(\xi,\eta)_{\eta=0}$	$f''(\xi,\eta)_{\eta=0}$	$f''(\eta)_{\eta=0}$
0.1	0.4444	0.4444	0.4447	0.4504	0.4504	0.4537
0.2	0.4451	0.4451	0.4457	0.4571	0.4570	0.4635
0.3	0.4458	0.4458	0.4467	0.4638	0.4636	0.4732
0.4	0.4464	0.4464	0.4477	0.4704	0.4702	0.4827
0.5	0.4470	0.4470	0.4487	0.4771	0.4768	0.4921

Table 2. Validation of results for various values of m with $Pr = 0.7, We = Ri = a = Rb = Nc = Nr = 0$.

	Mehmood et al.[11]	Iqbal et al.[12]	Present work
ξ	$-\theta\prime(\xi,0)$	$-\theta\prime(\xi,0)$	$-\theta\prime(0)$
0.1	0.3492	0.3417	0.3407
0.2	0.3342	0.3342	0.3327
0.3	0.3266	0.3266	0.3252
0.4	0.3188	0.3188	0.3182
0.5	0.3110	0.3110	0.3117

Table 3. For validation purposes, the current results are compared with previously reported data corresponding to the case $\mathrm{Pr} = 0.7,\ m = 0.5,\ Ri = a = Rb = Nc = Nr = 0$.

$$C_f = 2\frac{\tau_w}{\rho U_\infty^2}, Nu = \frac{q_w l}{k\,(T_w - T)}, Sh = \frac{j_w l}{D_s\,(C_w - C)}, NSh = \frac{j_{np} l}{D_B\,(_w -)} and Q = \frac{j_n l}{D_n\,(M_w - M)}. \quad (24)$$

where τ_w, q_w, j_w, j_{np} and j_n Represent, in order, the wall shear stress, heat transfer, solutal mass transfer, nanoparticle flux, and motile microorganism flux.

Introducing the dimensionless variables defined in (Mehmood et al.[11], Iqbal et al.[12]), and Eq. (24) is reformulated into its corresponding dimensionless form, yielding the PDEs as follows:

$$\left.\begin{array}{c} C_f = \frac{\sqrt{1+\frac{2}{x}}u_y}{1+\left(We\left(1+\frac{2}{x}\right)u_y\right)^n}, Nu = -\sqrt{1+\frac{2}{x}}_y, Sh = -\sqrt{1+\frac{2}{x}}_y \\ NSh = -\sqrt{1+\frac{2}{x}}h_y, Q = -\sqrt{1+\frac{2}{x}}_y \end{array}\right\}. \quad (25)$$

By inserting Eq. (17) into Eq. (25), the system is reduced to a set of ODEs. The drag force, Nusselt number, nanoparticle Sherwood number, mass transfer rate, and motile microorganism density number are subsequently formulated in terms of the Reynolds number (Re) as follows:

$$C_f(\xi Re)^{1/2} = \frac{\sqrt{(1+\sigma_x^2)}f''(0)}{1+\{We A\xi^{-0.5}f''(0)\}^n}, \quad (26)$$

$$NuRe_\xi^{-1/2} = -\sqrt{(1+\sigma_x^2)}\theta'(0), \quad (27)$$

$$NShRe_\xi^{-1/2} = -\sqrt{(1+\sigma_x^2)}h'(0), \quad (28)$$

$$ShRe_\xi^{-1/2} = -\sqrt{(1+\sigma_x^2)}\varphi'(0), \quad (29)$$

$$QRe_\xi^{-1/2} = -\sqrt{(1+\sigma_x^2)}\chi'(0). \quad (30)$$

Validation of the present results

To ensure the accuracy as well as reliability of the present numerical results, a systematic comparison was conducted with previously published data from the literature. In particular, Table 2 and Table 3 present a comparative evaluation of the values of f′′(0) as well as−θ′(0) with those reported by (Mehmood et al.[11] and Iqbal et al.[12]). The close agreement observed between the present findings and the published results demonstrates the accuracy, precision, and dependability of the current numerical method, validating its suitability for analyzing the boundary layer problem. Prior to making this comparison, a detailed grid-independence study was carried out to confirm that the numerical solution is not affected by the discretization in the η-direction. Several step sizes were tested as well as the resulting values of the skin-friction $(\mathrm{C_fRe_\xi^{0.5}})$, the Nusselt number $(\mathrm{NuRe_\xi^{-0.5}})$ as well as the Sherwood number $(\mathrm{ShRe_\xi^{-0.5}})$ were closely monitored for each refinement level. From these tests, it was observed that the computed values of $\mathrm{C_fRe_\xi^{0.5}}$, $\mathrm{NuRe_\xi^{-0.5}}$ as well as $\mathrm{ShRe_\xi^{-0.5}}$ stabilized up to an accuracy of 10^{-1}, indicating that further refinement

of the grid would not lead to significant changes in the results. To further verify this, simulations were performed using uniform grids of 100, 500. 1000 as well as 3000 points in the η-direction. In addition to grid refinement, the computational domain was truncated at η = 15, which was found to be sufficiently large to approximate the boundary at infinity. At this location, all dependent variables reached their asymptotic values smoothly, confirming that the chosen domain size is adequate for capturing the full boundary layer behavior and ensuring numerical stability. By combining the grid-independence tests, the careful selection of the computational domain, and the comparison with previously published results, it is evident that the numerical method employed is both robust and reliable. Consequently, the results presented in Table 4 can be considered grid-independent, accurate, and suitable for further analysis of the physical phenomena under consideration.

Solution methodology

An improved bvp4c strategy is employed to solve the boundary-value problem arising from the governing ODEs. Since the classical bvp4c solver often fails to converge when the initial guess is insufficiently close to the true solution as well as because the boundary-layer thickness is not known beforehand the proposed approach begins by computing the solution within a relatively thin boundary layer. The resulting profile is then used to update the initial guess, after which the computational domain is gradually expanded until a stable and accurate solution is obtained, as illustrated in Fig. 2a**.** This enhanced procedure offers several benefits: it significantly increases convergence reliability, eliminates the need for prior estimation of boundary-layer thickness, improves numerical stability by avoiding stiffness associated with large initial domains, and yields higher-accuracy solutions with reduced computational failures. Owing to its adaptive and robust nature, the method is broadly applicable to complex boundary-layer and multiscale boundary-value problems.

$$\begin{aligned}(s_1 = f, s_2 = f', s_3 = f'', s_3' = f''', s_4 = \theta, s_5 = \theta', s_5' = \theta'', s_6 = h),\\ (s_7 = h', s_7' = h'', s_8 = \varphi, s_9 = \varphi', s_9' = \varphi'', s_{10} = \chi, s_{11} = \chi', s_{11}' = \chi'').\end{aligned} \tag{31}$$

As described below, Eqs. (18–22) are reformed into an analogous set of 1st order ODEs;

$$\begin{aligned}s_3' = &\frac{\left(1+\left(We\left(1+a^2\pi^2\cos^2(\pi\xi)\right)\xi^{\frac{-1}{2}}s_3\right)^n\right)^2\left(-0.5s_1s_3-\frac{\xi a\pi^2\cos(\pi\xi)\sin(\pi\xi)s_2^2-\xi m s_2}{1+a^2\pi^2\cos^2(\pi\xi)}\right)}{\left(1+a^2\pi^2\cos^2(\pi\xi)\right)\left[1+(1-n)\left(We\left(1+a^2\pi^2\cos^2(\pi\xi)\right)\xi^{\frac{-1}{2}}s_3\right)^n\right]}\\ &-\frac{\left(1+\left(We\left(1+a^2\pi^2\cos^2(\pi\xi)\right)\xi^{\frac{-1}{2}}s_3\right)^n\right)^2\left(\frac{(Ri(s_4+Ncs_8-Nrs_6-R_bs_{10}))}{\left(1+a^2\pi^2\cos^2(\pi\xi)\right)}\right)}{\left(1+a^2\pi^2\cos^2(\pi\xi)\right)\left[1+(1-n)\left(We\left(1+a^2\pi^2\cos^2(\pi\xi)\right)\xi^{\frac{-1}{2}}s_3\right)^n\right]},\end{aligned} \tag{32}$$

$$s_5' = \frac{-0.5\,\mathrm{Pr}\,s_1s_5}{1+a^2\pi^2\cos^2(\pi\xi)}, \tag{33}$$

$$s_7' = \frac{-0.5Les_1s_7}{1+a^2\pi^2\cos^2(\pi\xi)}, \tag{34}$$

$$s_9' = \frac{-0.5Lns_1s_9}{1+a^2\pi^2\cos^2(\pi\xi)}, \tag{35}$$

$$s_{11}' = \frac{-0.5Scs_1s_{11}+ScPe\left(1-a\pi\cos(\pi\xi)\right)\left(\left(A+s_{11}\right)s_7'+Scs_7s_{11}\right)}{1+a^2\pi^2\cos^2(\pi\xi)}. \tag{36}$$

With BCs are

$$\begin{aligned}s_1(0)=0, s_2(0)=1, s_4(0)=1, s_6(0)=1, s_8(0)=1, s_{10}(0)=1,\\ s_2(\infty)=0, s_4(\infty)=0, s_6(\infty)=0, s_8(\infty)=0, s_{10}(\infty)=0\end{aligned} \tag{37}$$

Mesh points along η with η fixed at 15	$C_f Re_\xi^{0.5}$	$Nu Re_\xi^{-0.5}$	$Sh Re_\xi^{-0.5}$
100	0.4137	0.8668	0.8668
500	0.4137	0.8668	0.8668
1000	0.4137	0.8667	0.8667
2000	0.4137	0.8667	0.8667
3000	0.4137	0.8667	0.8667

Table 4. Grid independence test for the computed solution under the conditions
$\mathrm{Ri} = 0.5,\ \mathrm{Nc} = 2.0,\ \mathrm{We} = 0.1,\ \mathrm{n} = 2,\ \mathrm{Pr} = 3,\ \mathrm{Ln} = 3,\ \mathrm{Nr} = 0.3,\ \mathrm{A1} = 0.02,\ \mathrm{Sc} = 3,\ \mathrm{a} = 0.2.$

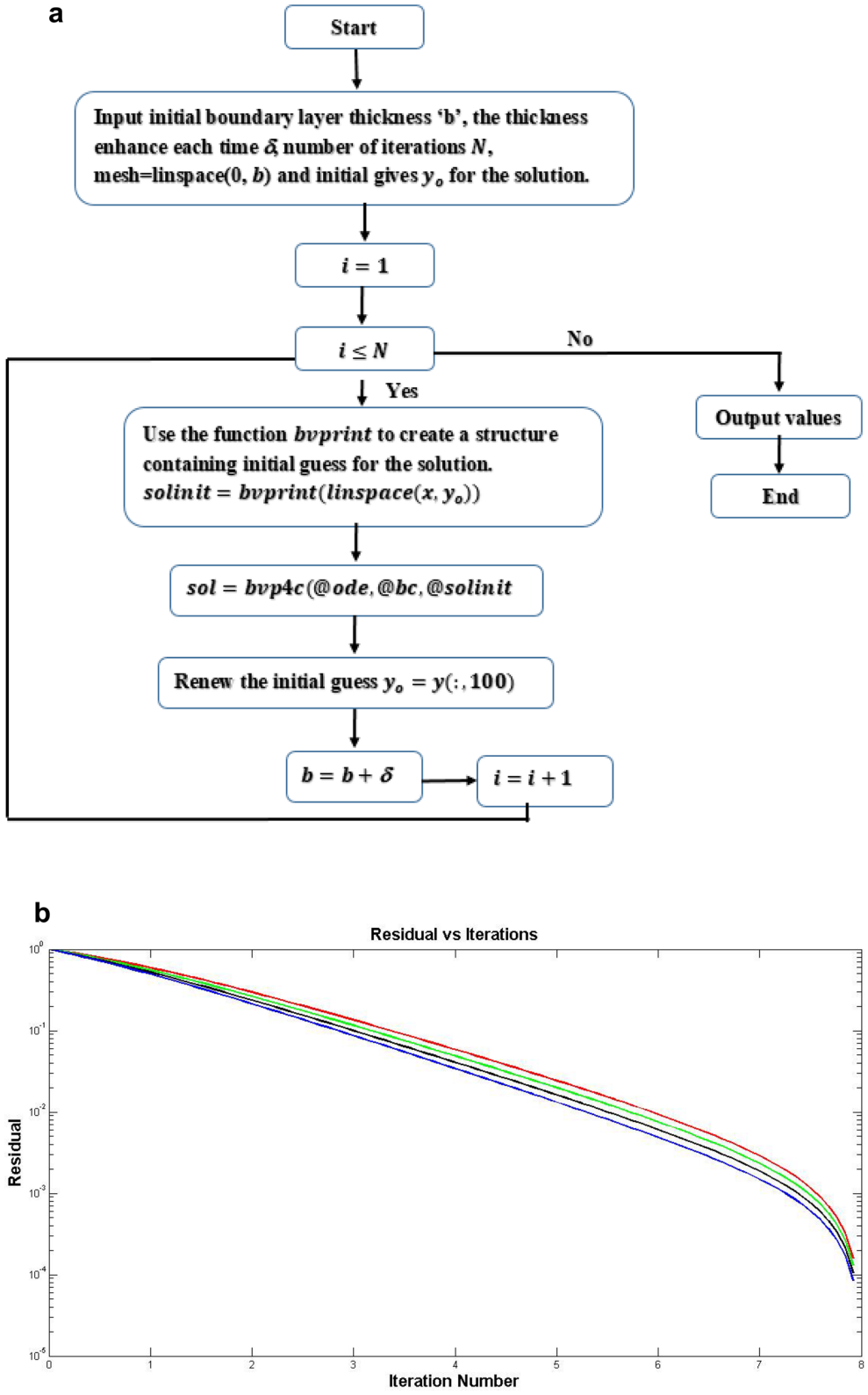

Fig. 2. (**A**) Flowchart illustrating the step-by-step algorithmic procedure setting. (**b**) Convergence behavior shown by plotting the residual values against iteration number for each case.

In addition, Fig. 2b illustrates the convergence characteristics of the numerical scheme by displaying the variation of the residual with respect to the iteration count for all examined cases. In this graph, the residual declines monotonically as the number of iterations grows, confirming the stability as well as robustness of the employed solution technique. The rapid drop in residual values during the initial iterations indicates that the iterative solver efficiently captures the dominant features of the solution. As the iteration progresses, the residual gradually approaches a very small magnitude, demonstrating that the computed solution is converging toward a steady state.

Results and discussion

This section provides a detailed study to examine the wavy properties of Cross magneto-fluid flow. Equations (20) and (22) define the impacts of microorganisms and bioconvection, and the boundary conditions are developed in combination with the governing flow Eqs. (18), (19), and (21). The Sherwood number (Sh), the density of motile microbes (Q), the Nusselt number (Nu), the Sherwood number of nanoparticles $(NShu)$ as well as the skin friction coefficient (C_f) are among the important dimensionless characteristics that are the subject of this investigation. To give a better understanding of the fluid behaviour under the combined effects of magnetic fields, non-Newtonian characteristics, nanoparticle transport, and microbial activity, these data are analysed and graphically depicted.

Figure. 3a–d illustrates the combined influence of magnetic field intensity as well as thermal diffusion on the flow characteristics by presenting streamline patterns for various values of the magnetic parameter (m) as well as the Peclet number (Pe). These visualizations highlight how changes in these parameters alter the flow structure and behavior. Enhancement of the magnetic parameter reinforces the Lorentz force, thereby suppressing the flow and reducing the velocity of the electrically conducting fluid. This damping effect diminishes the circulation strength as well as compresses the streamlines toward the central region, indicating a more restricted flow pattern. Conversely, changes in the Peclet number, which quantifies the relative importance of convective (advective) heat transfer compared to thermal diffusion have a pronounced effect on the thermal boundary layer thickness and, as a result, markedly impact the overall flow dynamics and temperature distribution. At lower Peclet numbers, thermal diffusion dominates, leading to smoother and more widely spaced streamlines. As the Peclet number increases, advective transport becomes more prominent, resulting in denser and more sharply curved streamlines, particularly near the heated surfaces. Figure 4**a–d** illustrates the isotherm contours for varying values of the Pr and the. At low Prandtl numbers, thermal diffusivity dominates, leading to broader as well as more diffused isotherms that extend deeply into the flow field. As the Prandtl number increases, the thermal boundary layer becomes thinner, and the isotherms cluster more closely near the heated surface, indicating steeper temperature gradients and reduced thermal diffusion. Simultaneously, increasing the magnetic parameter results in the suppression of convective motion due to the Lorentz force, which dampens fluid velocity and thus hinders the transport of heat by convection. This magnetic damping causes the isotherms to become more vertically aligned and uniformly spaced, reflecting a dominance of conduction over convection. Figure 5**a–e** illustrate the impact of the m on $C_fRe^{0.5}$, $NuRe^{-0.5}$, $ShRe^{-0.5}$, $NShRe^{-0.5}$ as well as Q $Re^{-0.5}$. It can be observed from Figs. 5**a–c** that elevating the m results in a reduction in the skin friction coefficient $\left(C_fRe^{0.5}\right)$, the Nusselt number $\left(NuRe^{-0.5}\right)$ which quantifies the rate of heat transfer as well as the Sherwood number $\left(ShRe^{-0.5}\right)$ indicating lower mass transport. This behavior is physically explained by the Lorentz force generated by the magnetic field. The applied magnetic field exerts a resistive influence on the electrically conducting fluid, slowing its motion as well as causing a thicker momentum boundary layer. As a consequence, the wall shear stress declines. The slower fluid movement also diminishes the temperature gradient at the surface, leading to a reduced rate of heat transfer. Similarly, the suppressed flow limits mass transport, causing a drop in the Sherwood number. Figure 5d indicates that the Sherwood number for nanoparticles $\left(ShRe^{-0.5}\right)$ boosts with $m.$, this is due to the accumulation of nanoparticles near the surface caused by the restricted flow and altered diffusion behavior. In Fig. 5e**,** as the m enhances, the density of motile microorganisms $\left(QRe^{-0.5}\right)$ declines. Physically, this occurs because the Lorentz force generated by the magnetic field opposes the fluid motion, slowing down the flow and suppressing the transport of microorganisms. As a result, fewer motile microorganisms reach the surface, leading to a reduction in their local density. The behavior of the Pe on the $C_fRe^{0.5}$, $NuRe^{-0.5}$,$ShRe^{-0.5}$, $NShRe^{-0.5}$ as well as $QRe^{-0.5}$ is portrayed in Fig. 6**a–e**. It is found that elevating the Peclet number leads to an overall enhancement in all these quantities. Specifically, the skin friction coefficient rises due to stronger convective transport, which accelerates fluid motion as well as reduces the momentum boundary layer thickness. The Nusselt number grows as the augmented convection strengthens thermal transport, steepening the temperature gradient at the surface. Similarly, the Sherwood numbers for both motile microorganisms as well as nanoparticles surge because higher Peclet number promotes mass transport, thinning the concentrationoundary layers as well as enhancing species flux. Consequently, the local density of motile microorganisms also amplifies, reflecting improved bioconvective accumulation near the surface. Figures 7**a–e** illustrate the influence of the bioconvection Rayleigh number (Rb) on $C_fRe^{0.5}$, $NuRe^{-0.5}$, $ShRe^{-0.5}$, $NShRe^{-0.5}$ as well as $QRe^{-0.5}$. It is observed from Figs. 6a–d that advancing Rb leads to a consistent minimize in $C_fRe^{0.5}$, $NuRe^{-0.5}$, $ShRe^{-0.5}$, $NShRe^{-0.5}$ as well as $QRe^{-0.5}$. Specifically, Fig. 7a shows that the $C_fRe^{0.5}$ declines with higher Rb, as the stronger bioconvective buoyancy forces induced by microorganism density variations are accompanied by more vigorous random motion of nanoparticles, which disrupts the organized fluid motion, reducing wall shear stress. Figure 7b indicates that the Nusselt number drops with elevating Rb the intensified thermal agitation of nanoparticles interferes with heat transport, lowering the temperature gradient at the surface. Figure 7**c, d** demonstrate that both $ShRe^{-0.5}$ and $NShRe^{-0.5}$ decrease as Rb rises, reflecting diminished mass transport of solute as well as nanoparticles due to chaotic motion that impedes coordinated upward swimming and diffusion processes. Finally, Fig. 7e shows that the density of motile microorganism $QRe^{-0.5}$ declines with increasing Rb, as the enhanced random motion of nanoparticles prevents microorganism accumulation near the surface, reducing their local density. Overall, a higher

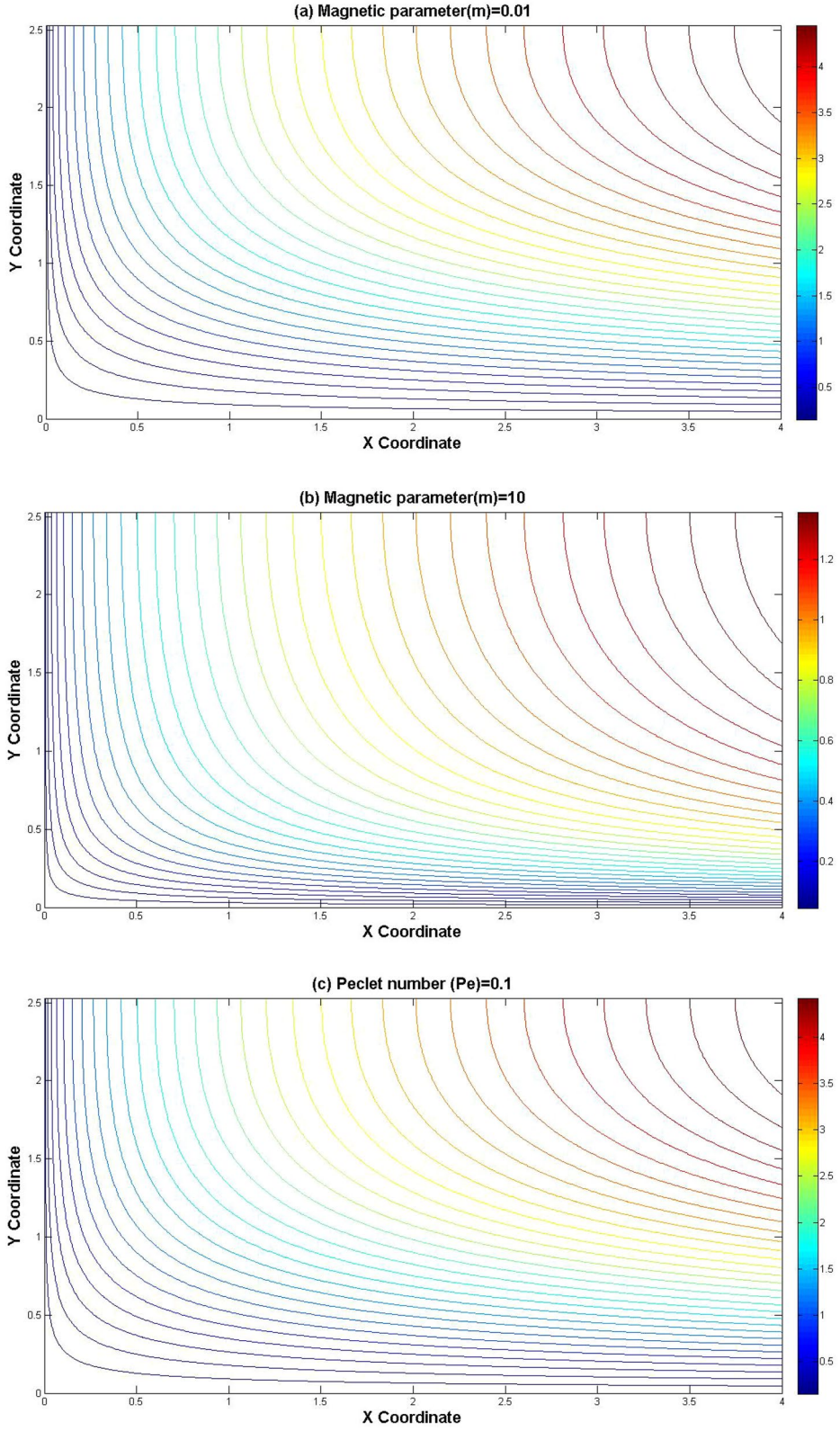

Fig. 3. **(a–d)** Streamlines for different values of m and Pe with Ri = 0.6, Nc = 0.2, We = 0.1, Ln = 2, Nr = 0.2, Rb = 0.3, Le = 0.3, n = 2, and Pr = 2.

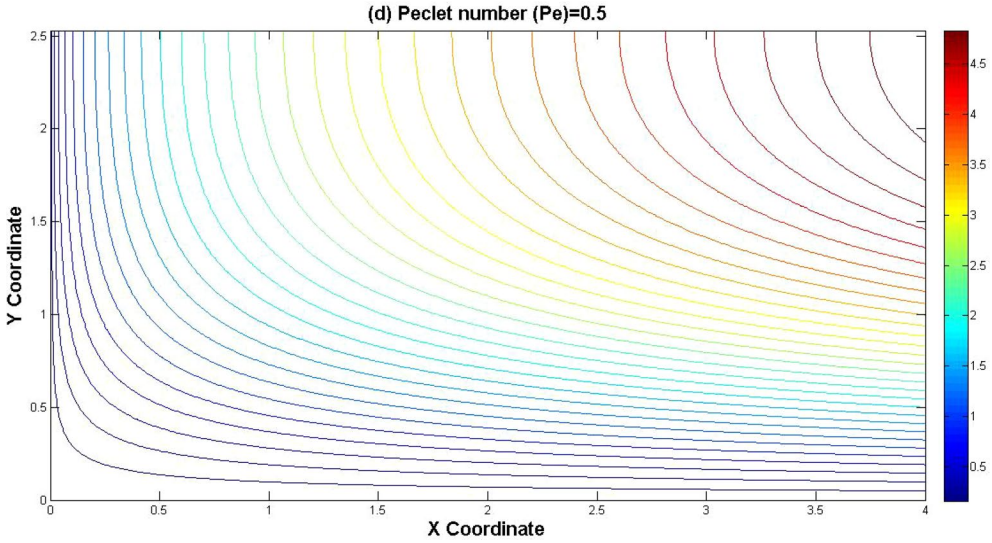

Fig. 3. (continued)

Conclusion

In this study, the mixed convection of Cross-type non-Newtonian fluid over a vertical wavy surface containing gyrotactic microorganisms was investigated, accounting for nanoparticle transport and bioconvection effects. The combined impacts of magnetic fields, Peclet number as well as bioconvection Rayleigh number on momentum, thermal transport as well as matter transport were analyzed. Enhancement of the magnetic parameter suppressed fluid flow via the Lorentz force, resulting in lower wall shear stress, heat transfer, and solutal mass flux, while promoting nanoparticle accumulation near the surface and reducing microorganism density. Higher Peclet numbers enhanced convective transport, leading to boost in skin friction, Nusselt number, Sherwood numbers, and microorganism density. Conversely, rising bioconvection Rayleigh numbers disrupted organized flow due to intensified random nanoparticle motion, resulting in diminished momentum, thermal as well as mass transfer as well as reduced microorganism accumulation.

Future research directions

The present study analyzed the behavior of a non-Newtonian fluid containing gyrotactic microorganisms over a wavy surface under the influence of magnetic and bioconvection effects. To further advance this research, several extensions can be explored to enhance the understanding of fluid systems, as outlined below.

- Extend studies to fully 3D flow to capture realistic patterns.
- Investigate the impact of double wavy or corrugated surfaces on transport processes.
- Explore density variations and compressibility effects on momentum, heat, and mass transfer.
- Analyze transient or time-dependent flows to understand dynamic behavior.
- Investigate Casson, Oldroyd-B, and other complex fluids.

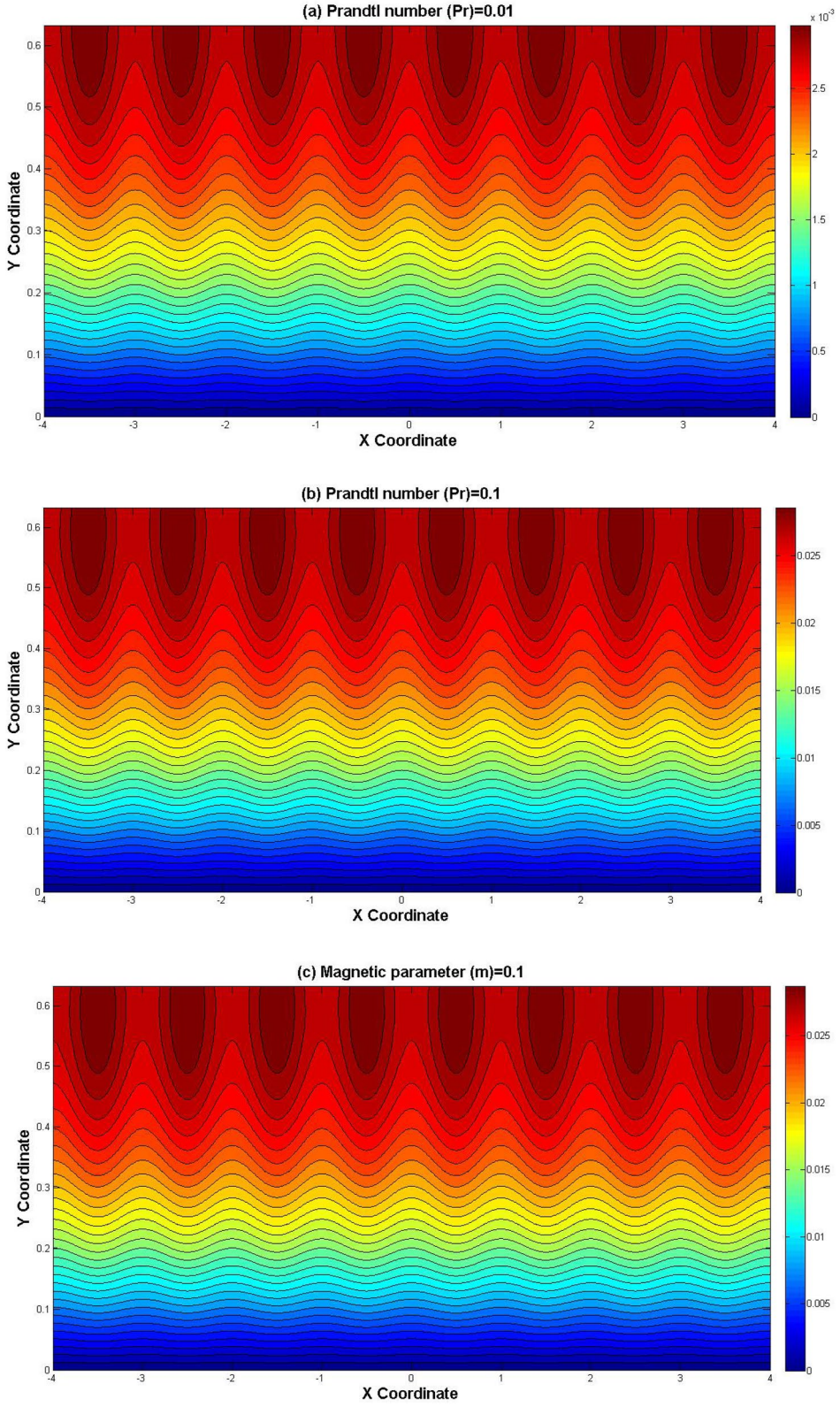

Fig. 4. **(a–d):** Isotherm contours for different values of Pr and m with Ri = 0.6, Nc = 0.2, We = 0.1, Ln = 2, Nr = 0.2, Rb = 0.3, Le = 0.3, n = 2, and Pe = 0.01.

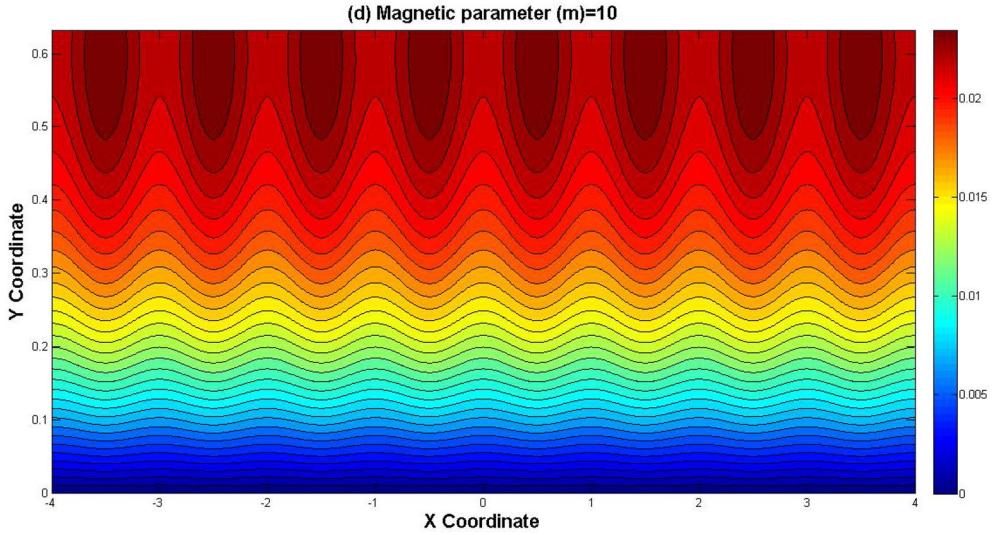

Fig. 4. (continued)

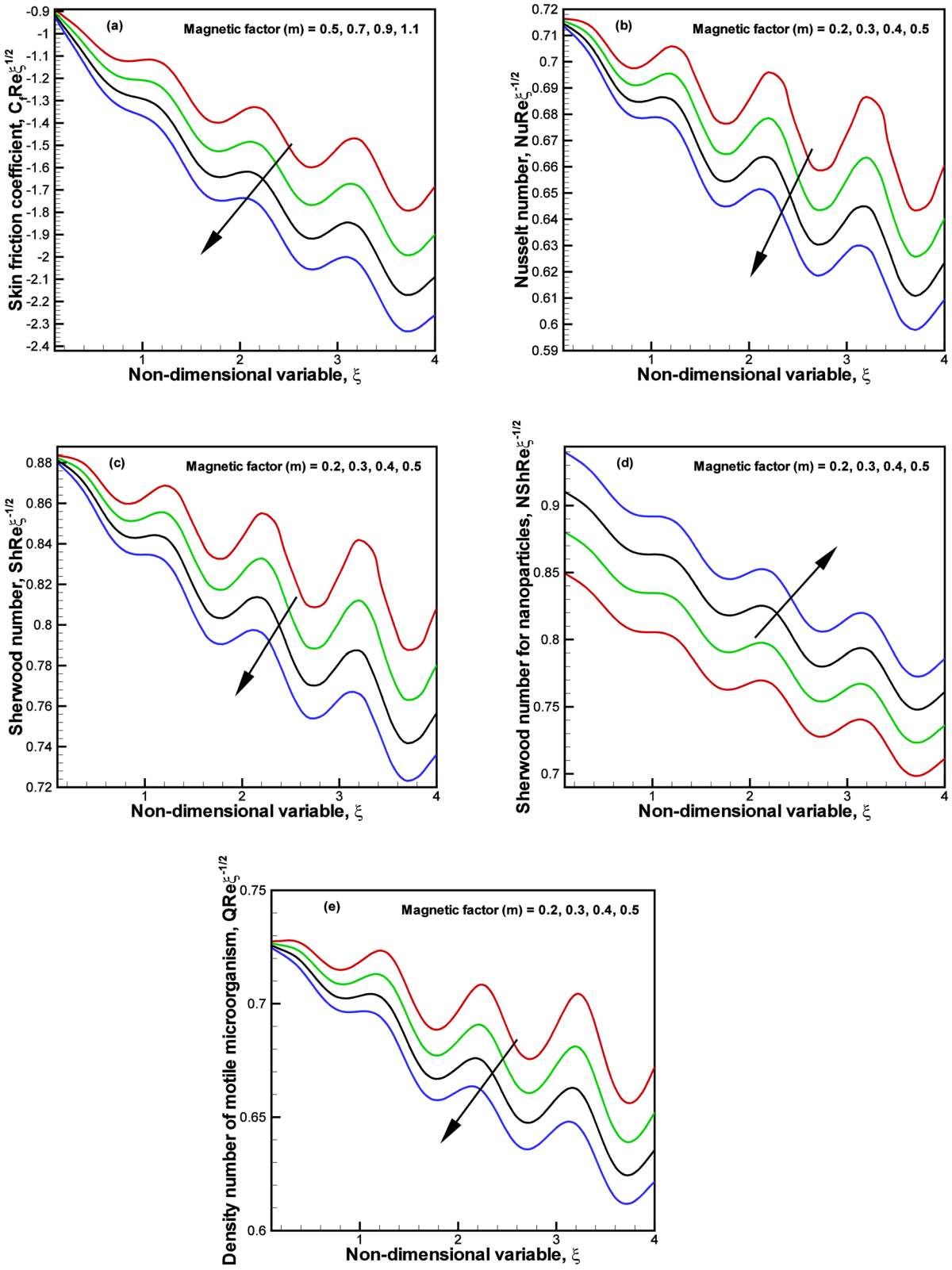

Fig. 5. **(a–e):** Variation of the skin friction coefficient (C_f), Nusselt number (Nu), Sherwood number (Sh), Sherwood number for nanoparticles (NSh) as well as Density number of motile microorganism (Q) with the parameter m, for Ri = 0.6, Nc = 0.2, We = 0.1, Pr = 2, Ln = 2, Nr = 0.2, Rb = 0.3, Le = 0.3, n = 2, and Pe = 0.01.

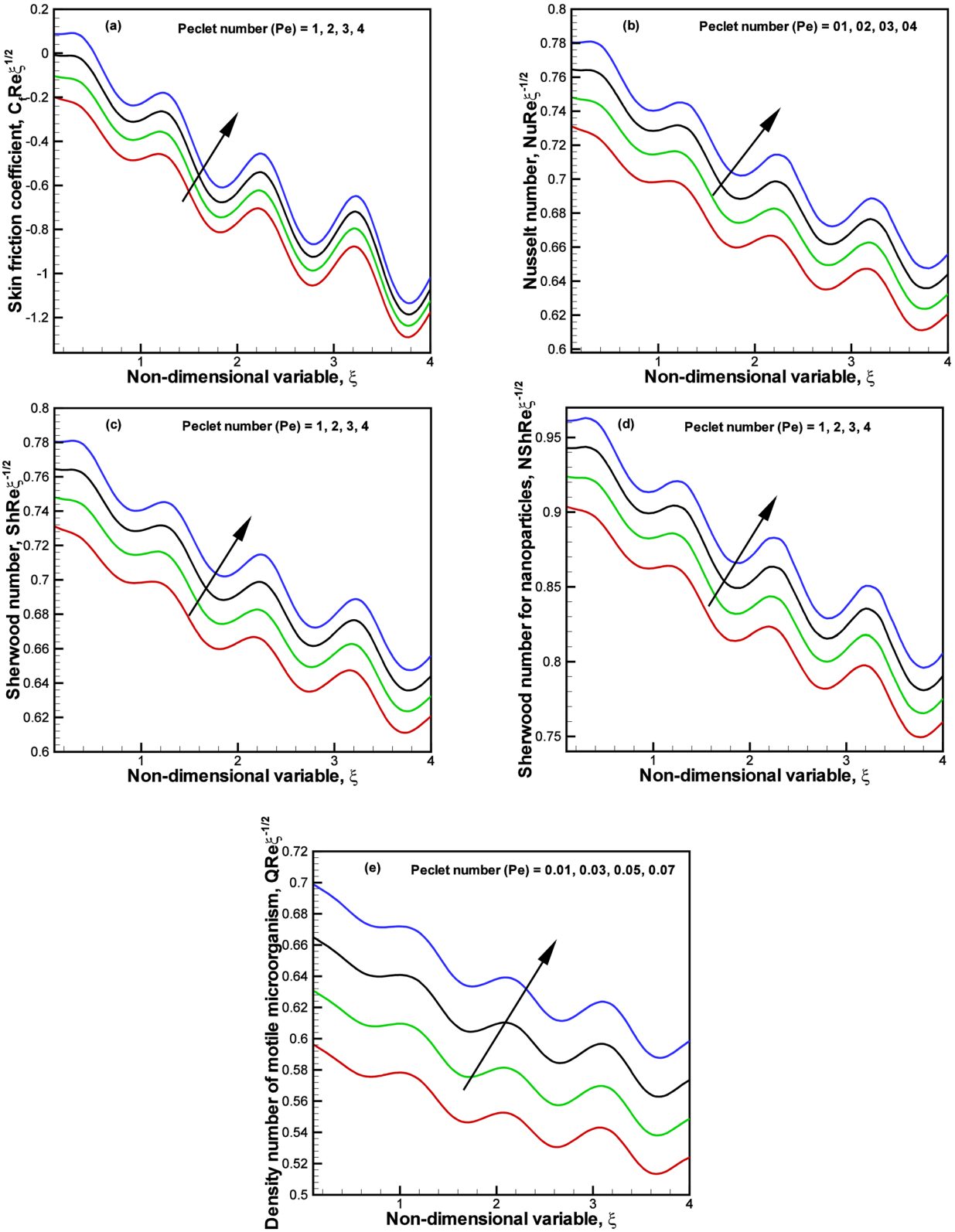

Fig. 6. **(a–e):** Influence of Pe on the skin friction, heat transfer, solutal transport, nanoparticle mass flux, and motile microorganism density for the parameter set Ri = 0.6, Nc = 0.2, We = 0.1, Pr = 2, Ln = 2, Nr = 0.2, Rb = 0.3, Le = 0.3, n = 2, and m = 0.1.

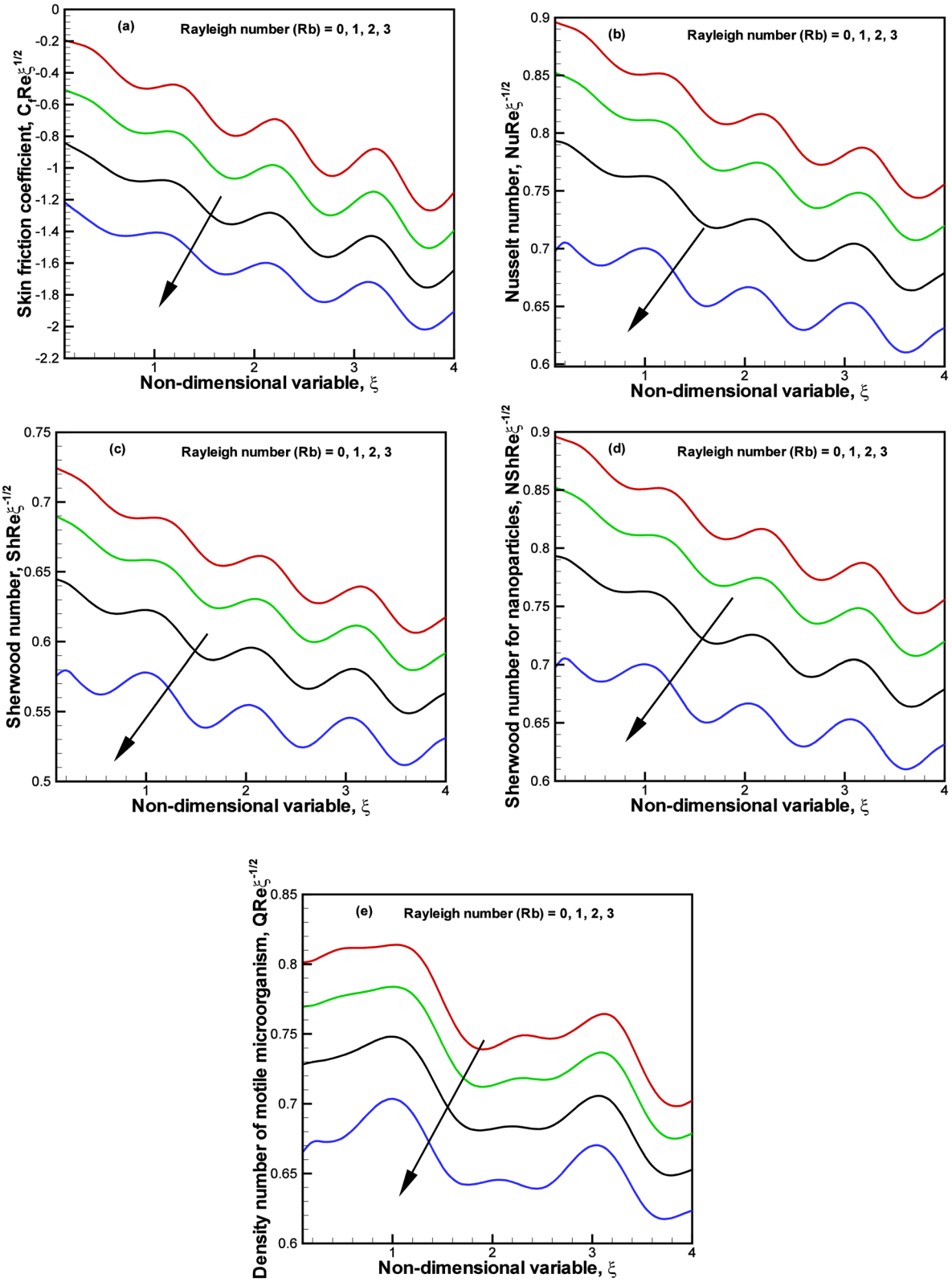

Fig. 7. **(a–e):** Influence of Rb on the skin friction, heat transfer, solutal transport, nanoparticle mass flux as well as motile microorganism density for the parameter set Ri = 0.6, Nc = 0.2, We = 0.1, Pr = 2, Ln = 2, Nr = 0.2, Pe = 0.01, Le = 0.3, n = 2, and m = 0.1.

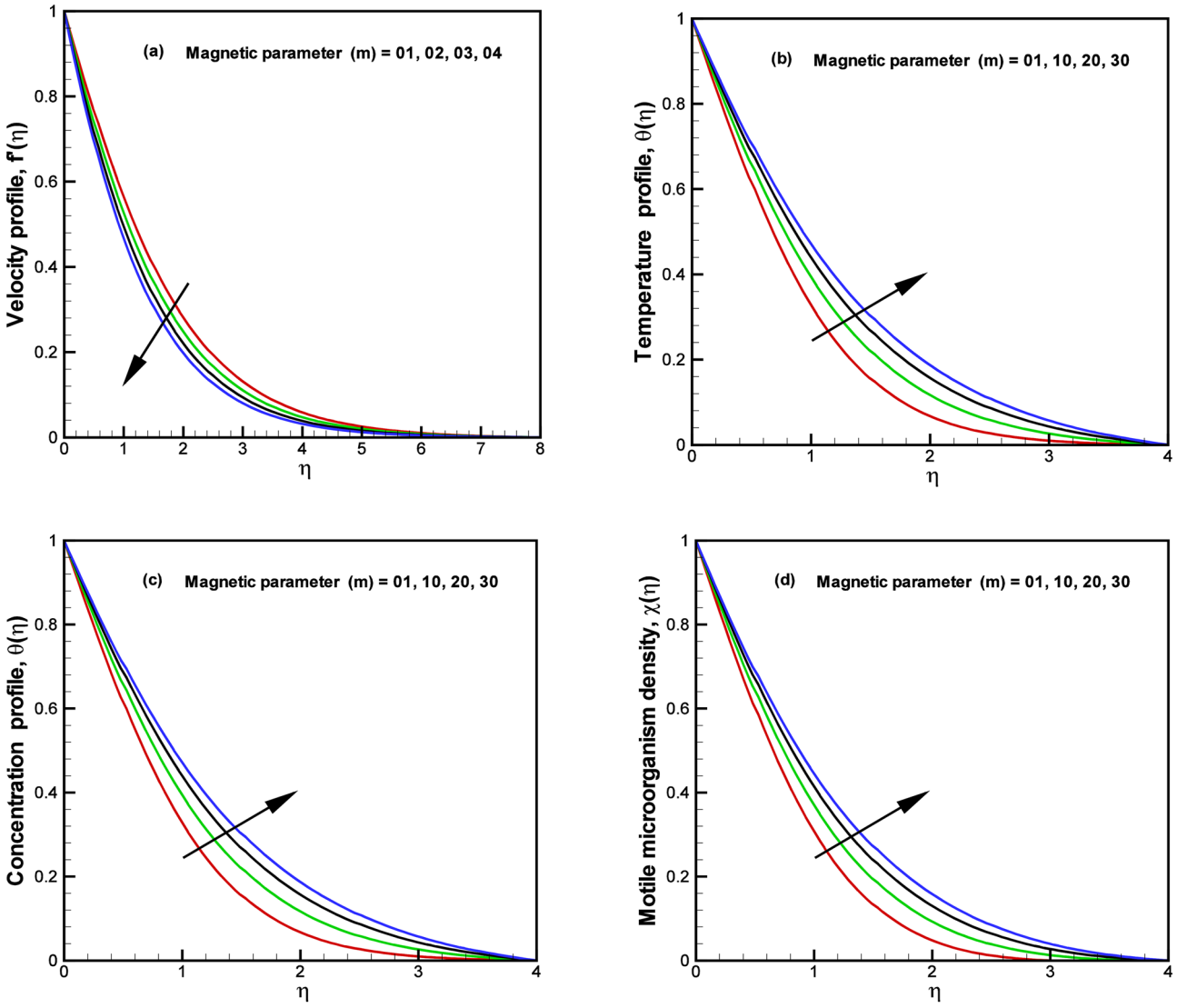

Fig. 8. **(a–d):** Variation of $f\prime(\eta)$, $\theta(\theta)$, $\phi(\eta)$ and $\chi(\eta)$ with m, for Ri = 0.6, Nc = 0.2, We = 0.1, Pr = 2, Ln = 2, Nr = 0.2, Pe = 0.01, Le = 0.3, n = 2, and Rb = 0.1.

Data availability

The datasets that support the results reported in this paper are accessible from the corresponding author on reasonable request.

Received: 19 October 2025; Accepted: 3 December 2025
Published online: 13 December 2025

References

1. Cross, M. M. Rheology of non-Newtonian fluids: a new flow equation for pseudoplastic systems. *J. Colloid Sci.* **20**(5), 417–437 (1965).
2. Nazeer, N. Numerical and perturbation solutions of cross flow of an Eyring-Powell fluid. *SN. Appl. Sci.* **3**, 1–11 (2021).
3. Sabir, Z. et al. A numerical approach for 2-D Sutterby fluid-flow bounded at a stagnation point with an inclined magnetic field and thermal radiation impacts. *Therm. Sci.* **25**(3), 1975–1987 (2021).
4. Escudier, M. P., Gouldson, I. W., Pereira, A. S., Pinho, F. T. & Poole, R. J. On the reproducibility of the rheology of shear-thinning liquids. *J. nonNewton Fluid Mech.* **97**(2–3), 99–124 (2001).
5. Ali, A. & Das, S. Applications of neuro-computing and fractional calculus to blood streaming conveying modified trihybrid nanoparticles with interfacial nanolayer aspect inside a diseased ciliated artery under electroosmotic and Lorentz forces. *Int. Commun. Heat Mass Transf.* **152**, 107313 (2024).
6. Adhikari, R., Das, S. & Das, S. Neural network-based simulation of microbial interactions in tetra-hybrid nanoparticles-enhanced cross blood streaming over stretchy artery stenosis considering magnetic and slip phenomena. Int. J. Model. Simul. 1–39 (2025).
7. Kumar, M. D., Shah, N. A., Gurram, D. & Yook, S. J. Predicting thermal transport of blood-based penta-hybrid nanofluid in Fin geometries using deep neural networks and finite difference approach. *Eng. Appl. Artif. Intell.* **162**, 112450 (2025).

8. Ghosh Moulic, S., Yao, L.S. Natural convection along a vertical wavy surface with uniform heat flux. *J. Heat Transf.* **111**(4) (1989).
9. Jang, J. H. & Yan, W. M. Mixed convection heat and mass transfer along a vertical wavy surface. *Int. J. Heat Mass Transf.* **47**(3), 419–428 (2004).
10. Wang, C. C. Mixed convection boundary layer flow on inclined wavy plates including the magnetic field effect. *Int. J. Therm. Sci.* **44**(6), 577–586 (2005).
11. Mehmood, A., Iqbal, M. S. & Mustafa, I. Cooling of moving wavy surface through MHD nanofluid. *Z Nat Forsch A*. **71**(7), 583–593 (2016).
12. Iqbal, M. S., Ghaffari, A., Riaz, A., Mustafa, I. & Raza, M. Nanofluid transport through a complex wavy geometry with magnetic and permeability effects. *Inventions* **7**(1), 7 (2021).
13. Acharya, N. On the hydrothermal behavior and entropy analysis of buoyancy driven magnetohydrodynamic hybrid nanofluid flow within an octagonal enclosure fitted with fins: Application to thermal energy storage. *J. Energy Storage* **53**, 105198 (2022).
14. Ahad, J. I., Hossain, A., Parvin, A. & Molla, M. M. Magnetohydrodynamics thermosolutal convection of hybrid MWCNT-Fe3O4-water nanofluid along a vertical wavy surface with wall heat and mass flux. *Partial Differ. Equ. Appl. Math.* **10**, 100667 (2024).
15. Zhang, Z. et al. Kinetic energetic exchange between near-inertial waves and mesoscale eddy/diurnal tide during typhoon rai. *J. Phys. Oceanogr.* **55**, 1033–1050 (2025).
16. Acharya, N. Effects of the curved fins on the entropy analysis and hydrothermal variations of Buoyancy-driven MWCNT-Fe3O4-H2O hybrid nanofluid flow within an annular enclosure. *Appl. Therm. Eng.* **269**, 126100 (2025).
17. Zhang, H., Wang, H., Zhou, X., Hu, J. & Zhou, B. Numerical investigation of a three-dimensional integrated system combining an inertial built-in wave energy converter array and a floating breakwater. *Energy* **326**, 136102 (2025).
18. Wager, H. W. T. VII. On the effect of gravity upon the movements and aggregation of Euglena viridis, Ehrb. and other micro-organisms. *Philos. Trans. R. Soc. Lond. B. Biol. Sci.* **201**, 333–390 (1911).
19. Ahmed, S. E. & Mahdy, A. Laminar MHD natural convection of nanofluid containing gyrotactic microorganisms over vertical wavy surface saturated non-Darcian porous media. *Appl. Math. Mech.* **37**(4), 471–484 (2016).
20. Srinivasacharya, D. & Ramana, K. S. Thermal radiation and double diffusive effects on bioconvection flow of a nanofluid past an inclined wavy surface. *Therm. Sci. Eng. Prog.* **22**, 100830 (2021).
21. Adhikari, R. & Das, S. Biological transmission in a magnetized reactive Casson-Maxwell nanofluid over a tilted stretchy cylinder in an entropy framework. *Chin. J. Phys.* **86**, 194–226 (2023).
22. Sarkar, S. & Das, S. Gyrotactic microorganisms swimming in magneto-Sutterby-nanofluid over a sliding cylinder set in a Darcy-Forchheimer porous space with Arrhenius kinetics. *Int. J. Amb. Energy* **45**(1), 2258896 (2024).
23. Adhikari, R. & Das, S. Exploring microbial dynamics in a reactive magnetised Casson-Maxwell-Oldroyd-B nanofluid on a slanted elongated cylinder: entropy assessment. *Int. J. Amb. Energy* **45**(1), 2367743 (2024).
24. Khan, D. et al. Effects of relative magnetic field, chemical reaction, heat generation and Newtonian heating on convection flow of Casson fluid over a moving vertical plate embedded in a porous medium. *Sci. Rep.* **9**(1), 400 (2019).
25. Muhammad, M. Y., Lawan, M. A. & Gambo, Y. Y. Heat absorption effect of magneto-natural convection flow in vertical concentric annuli with influence of radial and induced magnetic field. *Sci. Rep.* **14**, 15165 (2024).
26. Ramasekhar, G., Ahmad, H., Ozsahin, D. U. & Alotaibi, M. F. Aviation aspects of engine oil conveying copper tiny particles embedded in a rotating disk with a binary chemical reaction. *Case Stud. Therm. Eng.* **63**, 105180 (2024).
27. Lei, Y., Dong, S., Liang, R., Xiang, S., Huang, Q., Ma, J. & Yao, C. Parallel Resonant Magnetic Field Generator for Biomedical Applications. *IEEE Trans. Biomed. Circuits Syst.* (2024).
28. Palencia, J. L. D., Dharmaiah, G., Wakif, A., Noeiaghdam, S., Fernandez-Gamiz, U. & Dinarvand, S. ANFIS-PSO analysis on axisymmetric tetra hybrid nanofluid flow of Cu-CNT-Graphene-Tio2 with WEG-Blood under linear thermal radiation and inclined magnetic field: A bio-medicine application. *Heliyon* **11**(1) (2025).
29. Bhattacharyya, S. et al. Magneto-hydrodynamic behavior of magnetic nanofluids in mini-channel heat sinks for electronics cooling. *Sci. Rep.* **15**(1), 28861 (2025).
30. MN, P., Gunisetty, R. & SK, N. Enhanced heat performances of penta-hybrid nanofluid flow across a stretching surface employing the homotopy perturbation method: An artificial neural network approach. *Phys. Fluids* **37**(7) (2025).
31. Kumar, M. D. et al. Forecasting heat and mass transfer enhancement in magnetized non-Newtonian nanofluids using Levenberg-Marquardt algorithm: Influence of activation energy and bioconvection. *Mech. Time Depend. Mater.* **29**(1), 14 (2025).
32. Ramasekhar, G., Divya, A., Selvi, P. D., Narayanagari, R., Sekhar Reddy, R. C., Jakeer, S. & Ahmed, S. F. Exploring the role of Casson hybrid nanofluid flow through a stretching cylinder with a significant impact of heat source/sink: A computational analysis. *AIP Adv.* **15**(3), (2025).

Acknowledgements

Acknowledgement: The authors extend their appreciation for the support received from Princess Nourah bint Abdulrahman University Researchers Supporting Project number (PNURSP2025R163), Princess Nourah bint Abdulrahman University, Riyadh, Saudi Arabia.

Author contributions

L.A; S.J: Conceptualization, Methodology, Software, Formal analysis, Validation; Writing—original draft. B.Z; H.O.H: Writing–original draft, Data curation, Investigation, Visualization, Validation. U.K: Conceptualization, Writing–original draft, Writing–review & editing, Supervision, Resources. N.S.K; S.E: Validation, Investigation, Writing–review & editing, Formal analysis; Project administration; Funding acquisition, software.

Declarations

Competing interests

The authors declare no competing interests.

Additional information

Correspondence and requests for materials should be addressed to H.O.H.